PCCP

ROYAL SOCIETY OF CHEMISTRY

COMMUNICATION

View Article Online
View Journal | View Issue

Cite this: *Phys. Chem. Chem. Phys.*, 2024, **26**, 47

Received 10th September 2023,
Accepted 20th November 2023

DOI: 10.1039/d3cp04386j

rsc.li/pccp

The light-dependent pseudo-capacitive charging of conjugated polymer nanoparticles coupled with the depolarization of the neuronal membrane†

Greta Chiaravalli,[ab] Tiziana Ravasenga,[cd] Elisabetta Colombo,[cd] Jasnoor,[ce] Simona Francia,[cd] Stefano Di Marco,[cd] Riccardo Sacco,[f] Grazia Pertile,[g] Fabio Benfenati *[cd] and Guglielmo Lanzani *[ab]

The mechanism underlying visual restoration in blind animal models of retinitis pigmentosa using a liquid retina prosthesis based on semiconductive polymeric nanoparticles is still being debated. Through the application of mathematical models and specific experiments, we developed a coherent understanding of abiotic/biotic coupling, capturing the essential mechanism of photostimulation responsible for nanoparticle-induced retina activation. Our modeling is based on the solution of drift-diffusion and Poisson–Nernst–Planck models in the multi-physics neuron-cleft-nanoparticle-extracellular space domain, accounting for the electro-chemical motion of all the relevant species following photo-excitation. Modeling was coupled with electron microscopy to estimate the size of the neuron-nanoparticle cleft and electrophysiology on retina explants acutely or chronically injected with nanoparticles. Overall, we present a consistent picture of electrostatic depolarization of the bipolar cell driven by the pseudo-capacitive charging of the nanoparticle. We demonstrate that the highly resistive cleft composition, due to filling by adhesion/extracellular matrix proteins, is a crucial ingredient for establishing functional electrostatic coupling. Additionally, we show that the photo-chemical generation of reactive oxygen species (ROS) becomes relevant only at very high light intensities, far exceeding the physiological ones, in agreement with the lack of phototoxicity shown *in vivo*.

1. Introduction

Degeneration of photoreceptors in the retina leads to visual impairment and eventually results in blindness in disorders such as retinitis pigmentosa (RP) and age-related macular degeneration. We have recently demonstrated that when injected within the subretinal space, organic photovoltaic nanoparticles (NPs) made of poly(3-hexylthiophene-2,5-diyl) (P3HT) can restore light sensitivity in blind rats.[1,2] Once injected and captured in the subretinal space, NPs establish tight contacts with the plasma membrane of retinal neurons spared by degeneration. Upon illumination, NPs transduce light into a bioelectrical signal that stimulates the second order retinal neurons, namely bipolar and horizontal cells, thus reactivating the visual path. Importantly, NPs are not internalized by neurons but adhere to their membrane.[2]

Light entering the eye is focused on the retina. In a healthy retina, photoreceptors located in the outer layer absorb light and hyperpolarize, phasically reducing their tonic synaptic glutamate release present in the dark. Bipolar cells in contact with photoreceptors respond to this modulation by starting a transduction cascade that reaches retinal ganglion cells (RGCs) in the inner retina, which funnel the signal into the optic nerve. In dystrophic retinas, photoreceptors are removed and the subretinally injected NPs decorate the surviving bipolar and horizontal cells.[1] When the impinging light hits the semiconducting NPs, we assume that an exponential concentration gradient of charge carriers (electrons and holes) is established in space according to the Lambert–Beer law. This implies assuming a uniform absorption coefficient within the polymer NP, as it is standard in polymer films. While local intensity fluctuations due to inhomogeneity are probably occurring within each NP, smoothing them out seems to be a practical approximation that does not compromise the quality of the phenomenon. The large asymmetry in carrier mobility causes the electrical polarization of the NPs according to the photo-Dember effect: hole diffusion spreads positive charges homogeneously, while electrons are essentially fixed.[4] At the illuminated side, where the negative charge accumulates, electrons transferring to hydrated oxygen generates a population of superoxide molecules that increases negative polarization, creating pseudo-capacitive charging.

[a] *Center for Nano Science Technology, Istituto Italiano di Tecnologia, Milano, Italy. E-mail: guglielmo.lanzani@iit.it*
[b] *Politecnico di Milano, Physics Department, Milano, Italy*
[c] *Center for Synaptic Neuroscience and Technology, Istituto Italiano di Tecnologia, Genova, Italy. E-mail: fabio.benfenati@iit.it*
[d] *IRCCS Ospedale Policlinico San Martino, Genova, Italy*
[e] *Department of Experimental Medicine, University of Genova, Genova, Italy*
[f] *Politecnico di Milano, Mathematics Department, Milano, Italy*
[g] *Department of Ophthalmology, IRCCS Sacrocuore Don Calabria Hospital, Negrar, Verona, Italy*

† Electronic supplementary information (ESI) available. See DOI: https://doi.org/10.1039/d3cp04386j

The bio-organic interface was found to be diffused on tens of nm, due to the surface swelling of the polymer, and consists of a quasi-virtual cleft (thickness <20 nm, as determined by FIB/SEM analysis[2]) at the contacts between NPs and the apical dendrites and cell bodies of bipolar cells. This region is a secluded space filled by proteins and characterized by a very low concentration of ions. The well-established formation of a protein corona around NPs in the physiological environment[5] has the essential feature of displacing free ionic charges at the interface that hamper electrical screening, favoring the formation of a tight electric coupling between the NP and the cell membrane that enhances the electrostatic effect induced by the accumulated charge. Each NP, acting as a nano-electrical synapse powered by light may induce a depolarization of a fraction of mV. However, the depolarization response of the bipolar cell is the result of temporal and spatial summation of individual membrane voltage changes caused by tens of NPs distributed along the neuronal membrane, as it occurs in any postsynaptic neuron in central chemical synapses.[6] This effect is particularly relevant for the vast majority of bipolar cells which do not have a threshold to be reached to trigger action potential firing, being unable to generate action potential. Rather, they function in an "analogic" fashion by releasing glutamate at the synapses with RGCs based on subthreshold oscillations of their membrane potential.[7] The depolarization integrated in time and space by the network of NPs yields a detectable membrane depolarization of bipolar cells and RGCs. This phenomenon has been proved to occur in the retina of blind rats and which mediates light restoration.[1,2]

The mechanism of photo-transduction that has been proposed in recent papers[1,2,8–10] is here validated by a numerical model. We will show that the "photochemical" mechanism, associated with the generation of ROS, can be disregarded under expected retina conditions, and that the electrostatic effect caused by the accumulated charge is responsible for the perturbation of local membrane potential. Furthermore, measurements on explanted retinas treated with NPs acutely or chronically support the theoretical suggestion highlighting the role of the dielectric cleft that is formed over time within the tissue. The proposed model will provide a complete quantitative description of the full system taken into consideration, providing quantitative prediction of the most relevant effect triggered by the photo-modulation of P3HT NPs.

2. Methods

2.1. Mathematical modeling

For our analysis, we used two mathematical models: a 3D model of the photo-Dember effect in the NP and a 1D model of the biophysical events taking place at the interface between the NP and the neuronal membrane. The 3D model focuses on

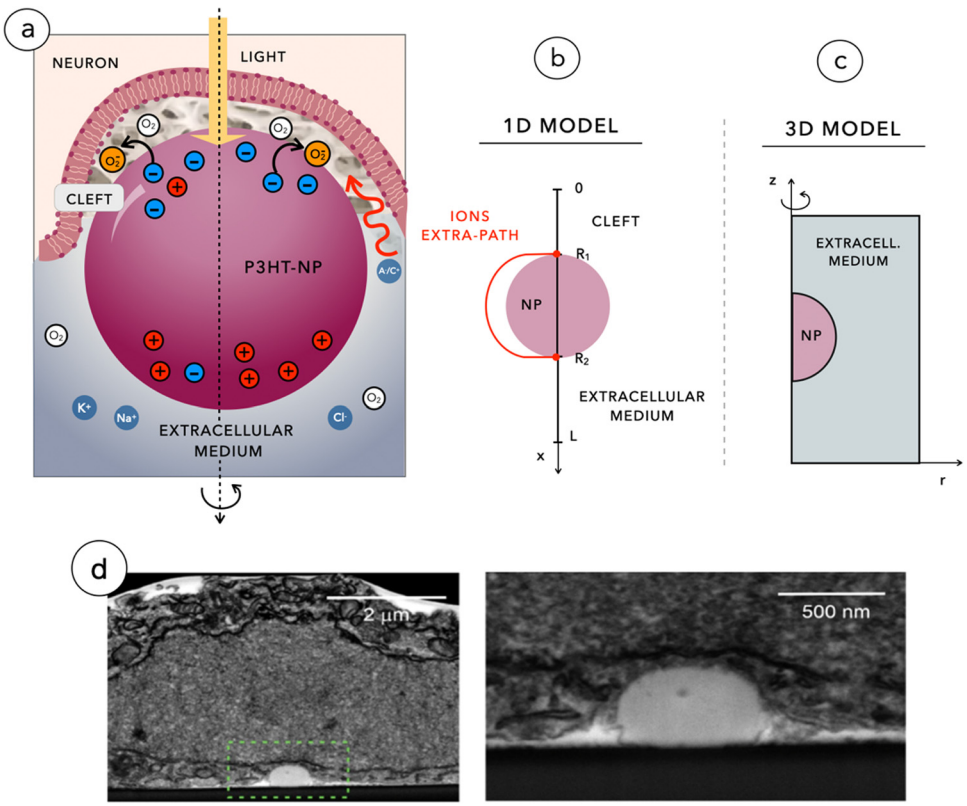

Fig. 1 (a) Cross-section of the 3D neuronal membrane engulfing the P3HT-NP, surrounded by a proteinaceous cleft region and by the extra-junctional electrolytic solution with its 3D representation in cartesian coordinates. (b) and (c) Geometrical scheme of the 2D-axial symmetric model (c) and of the 1D reduced model (b). (d) Low and high magnification images of the NP–neuron contact obtained from FIB/SEM analysis. The junctional neuronal membrane wraps the NP forming a quasi-virtual cleft.

the study of the sole NP by considering the three-dimensional redistribution of charges across the spherical domain, leading to a non-uniform polarization of NPs. The 1D model instead aims at reproducing the full photo-transduction mechanism depicted in Fig. 1a and imaged through FIB/SEM as shown in Fig. 1d.

Both simulations are based on the resolution of a system of partial differential equations (PDEs) according to the Poisson–Nernst–Planck model with the use of a fixed-point iteration algorithm, in the framework of the classic Gummel's map algorithm. Besides being computationally efficient, the fixed-point iteration has also the significant advantage of favoring the use of the most appropriate discretization schemes to approximate the dependent variables of the problem. In particular:

• Piecewise linear finite elements with mass lumping stabilization[11] are used to numerically solve the PDEs. This prevents the occurrence of non-physical oscillations in the spatial distribution of the electric potential, especially in the neighborhood of material interfaces;

• Piecewise linear finite elements with Scharfetter-Gummel stabilization[12] are used to numerically solve the continuity equations for carriers and ions. This preserves on the discrete level the strict positivity of the carrier number densities and ion molar density.

The 3D nanoparticle model. Fig. 1a shows a schematic illustration of the abiotic/biotic interface, characterized by rotational invariance with respect to the z-axis, parallel to the incoming light direction (yellow arrow): this evidence allows us to reduce the 3D system (in a Cartesian reference system) into a 2D axial symmetric (2DAS) structure depicted in Fig. 1c, in the r–z coordinate system, without losing generality. The 2DAS region, which is the computational domain of our model, is the union of the NP subdomain Ω_1 and of the subdomain Ω_2 representing the aqueous extracellular environment surrounding the NP. It is important to notice that 2DAS reduction does not hamper the accuracy of the description, which remains equivalent to a 3D resolution of the system. In the 2DAS model, we solve a stationary version of the classical drift diffusion equation inside Ω_1, representing the NP, and the Poisson equation for the electric field and potential across the whole domain Ω. The NP model accounts for the Lambert–Beer generation of holes and electrons, the Shockley–Read–Hall (SRH) trap-assisted recombination and Marcus–Gerischer interface photo-cathodic reaction of electrons with the molecular oxygen dissolved in the environment. All equations and parameters are reported in the study by Chiaravalli *et al.*[4,13] and in the supplementary material (ESI).† The NP is immersed in an empty medium, notably without ions. This allows to focus on the NP under illumination, excluding ionic screening effects. These are indeed important and will be studied in the 1D model, presented in the next paragraph.

The 1D nanoparticle-cleft model. Fig. 1b shows the 1D computational domain comprising the cleft region $(0,R_1)$, the NP (R_1, R_2) and the extracellular medium (R_2,L), with an extra path connecting the electrolyte to the cleft region (red in the figure) allowing ions to diffuse and penetrate the secluded cleft space. In this model, we solve a time-dependent problem that includes the drift diffusion equations across the NP region and the modified version of the Poisson–Nernst–Planck system (as described in the ESI†) across the cleft/extracellular region and across the extra-path. The coupled resolution of Poisson and Nernst–Planck equations is coherent with the available literature dealing with electrodiffusion at the membrane level.[14,15] We account for the presence of all bulk ions in the electrolyte, in particular Na^+, K^+, Cl^- and the superoxide O_2^-, which results from the oxidation of negative polarons in the photoexcited NP by molecular oxygen dissolved in the environment. At $z = 0$, we also account for the presence of neurons by introducing boundary conditions consistent with the Goldman–Hodgkin–Katz expressions for ionic transmembrane currents. All equations and parameters can be found in the ESI.†

2.2. Experimental techniques

Electron microscopy and focused ion beam preparation of the NP–neuron interface. Primary cortical neurons were prepared from C57BL/6J mouse embryos (Charles River) as reported previously.[3] Briefly, mice were sacrificed by CO_2 inhalation, and the embryos were removed by cesarean section. After enzymatic dissociation, cells were plated on glass coverslips drop-casted with P3HT-NPs and incubated for 14 days. P3HT-NPs water suspensions were prepared using the reprecipitation method involving an organic solvent and had an average hydrodynamic diameter of $\sim$200 nm, as described previously.[1,3] All animal manipulations comply with European and Italian regulations (Directive 2010/63/EU of March 4th, 2014). Neurons were fixed using a glutaraldehyde solution in sodium cacodylate buffer at room temperature, stained using a RO-T-O protocol, a uranyl acetate treatment, a staining of the cytoskeleton, and were finally embedded in resin.[1] After resin polymerization, a thin gold layer was deposited on the samples by plasma sputtering for the grounding of the preparation. Cross-sectional imaging of the neuron/NP samples was realized using a dual beam Helios Nanolab 650 equipment (Thermo Fisher) as described previously.[1] After further coating with a thin platinum layer to protect the preparation from the ion beam, neurons were cut using the focused ion beam (FIB) with an ionic current >9 nA (30 kV) to reveal the interface between the cell and the NP. A final polishing of the surface was performed to achieve a clearer view of the cell interior. Scanning electron microscopy (SEM) images were acquired at a tilt angle and 3 kV. The colors of the SEM images were inverted to highlight the cellular components.

Ethical approval and animal handling. All animal handling and experimental protocols were performed in compliance with the guidelines established by the European Community (Directive 2014/26/EU of 4 March 2014) and were approved by the local IRCCS Ospedale Policlinico San Martino ethical committee and the Italian Ministry of Health (Authorization # 357/2019-PR). Inbred Royal College of Surgeons pink-eyed dystrophic (RCS) animals, together with congenic non-dystrophic

(rdy) controls were kindly provided by Dr M. M. La Vail (Beckman Vision Center, University of California San Francisco, CA). Rat colonies were bred under standard conditions with *ad libitum* access to food and water under a 12/12 h light/dark cycle. Experimental groups were randomly selected maintaining a balance of female and males.

***In vivo* subretinal injection of NPs.** Royal College of Surgeons (RCS) rats (12/15 months old), bearing a loss-of-function mutation in the *Mertk* gene causing photoreceptor degeneration, were anesthetized with diazepam (Ziapam, Ecuphar; 5 mg kg^{-1}) by intraperitoneal administration followed by intramuscular injection of xylazine (Rompun, Bayer; 5 mg kg^{-1}) and ketamine (Lobotor, Acme; 50 mg kg^{-1}). After pharmacological pupil dilation, a 2 mm cut of the conjunctiva in the temporal eye allowed a 1 mm incision through the sclera and choroid. The retina was gently detached by an injection of viscoelastic material, followed by an injection of P3HT-NPs in subretinal position, as described before.[3] Tissues were sutured by thermally assisted coagulation. Antibiotic and corticosteroid eye-drops (TobraDex 0.3% + 0.1%, Alcon) were applied to prevent post-surgery inflammation and/or infection.

Multielectrode array recordings of retinal explants. Dystrophic retinas were dissected from the enucleated eyes of RCS rats which were either untreated (control) or injected *in vivo* with NPs 30 days before (chronic condition). Eyes were cleared of the residues of conjunctiva and sclera, while the choroid was left intact. Tissues were continuously perfused with carbo-oxygenated Ames medium. Each eye was divided into smaller pieces of about 1–2 mm side, able to cover the whole active surface of a 60-electrode multielectrode array (MEA; MultiChannel Systems) in which explants were positioned in epiretinal configuration (RGCs in contact with microelectrodes). Explants from non-injected RCS rats were employed to perform an *in vitro* injection of P3HT-NPs between the choroid and the inner retina under a stereomicroscope to acutely mimic the *in vivo* surgery (acute condition). Light-evoked extracellular recordings were obtained using a fiber-coupled Lumencor LED system (Spectra X) peaking at 530 nm fed to an inverted Nikon Eclipse Ti microscope, with an illumination spot of $\sim$1 mm^2 and a power density of 20 mW mm^{-2}. Light pulses of 200 ms duration were administered 25 times at 0.25 Hz for each condition. Only retinal explants where P3HT-NP intrinsic fluorescence was detected concomitantly with the recording were included in the analysis to ensure a correlation between the presence of the photoactive material and the firing modulation of RGCs. Data were acquired at 25 kHz and were high band-pass filtered at 200 Hz. Spike detection was performed using MC Rack software (multi channel systems) and the analysis of the firing frequency was performed using Origin Pro 2020 and GraphPad Prism 9.1.2. Post-stimulus time histograms (PSTHs) were realized for each electrode with a threshold of 0.8 Hz basal firing activity, with a spike detection threshold set at 4 standard deviations from the noise. Light-evoked firing activity was assessed by selecting those electrodes showing a statistically significant modulation of firing with respect to the baseline that was time-locked to the light stimulus.

2.3. Statistics

The sample size needed for the planned experiments (n) was predetermined using the G*Power software for the ANOVA test with three experimental groups, considering an effect size = 0.25–0.40 with alpha (type-I error) = 0.05 and 1-β (type-II error) = 0.9, based on similar experiments and preliminary data. Peri-Stimulus Time Histograms (PSTHs) were realized with a 20 ms bin size and each bin is expressed by mean ± SEM. Data are represented as box plots, where the line depicts the median, the box extends from 25th to 75th percentile of the population, and the whiskers show the Tukey's limit for outliers definition. Normal distribution was assessed using D'Agostino–Pearson normality test, and one-way ANOVA followed by the Tukey's multiple comparison test was used. $p < 0.05$ was considered statistically significant.

3. Results and discussion

According to the proposed model, we consider two phenomena that may occur at the neuron–NP interface: (i) the photoelectrostatic effect, due to the electric potential generated by the light-induced Dember polarization of the NP; (ii) the photochemical effect, which consists in the activation of cellular pathways secondary to the interaction of the membrane with O_2^-, produced at the interface with the NP. The NP polarization, according to the Dember effect, appears upon considering the Lambert–Beer carrier generation profile in space and the strongly asymmetric transport of electrons and holes inside the NP, as modeled and validated against electrochemical studies on P3HT thin films.[4] To accurately account for this effect, we have studied it using a 2DAS model of the NP.

The photo-chemical effect is accounted for in the 1D model by the introduction of boundary conditions for electron and O_2^- continuity equations at the interface between the NP and the external environment. The photo-cathodic reaction rate $O_2 + e^- \rightarrow O_2^-$ is described using the Marcus–Gerischer equation. In addition, to reproduce the long-lasting effect of P3HT-based retinal NP implants and their ability not to degrade over time, the 1D model accounts for a hole-surface-recombination effect, promoted by the presence of accumulated negative O_2^- at the interface.

3.1. The photo-Dember effect

Fig. 2a shows the multidimensional drift-diffusion steady-state simulation of the charge density distribution in a NP with a radius of 150 nm irradiated from the bottom with a light power of 2×10^{-1} W m^{-2}, estimated to be the physiological light intensity impinging onto the retina[16] under normal daylight illumination conditions. Fig. 2b illustrates the net charge density profile across the NP, obtained using the 1D-model in a time-dependent simulation. Both models consistently indicate the formation of a dipole-like charge distribution, due to the difference in mobility between electrons, with a mobility of $\mu_n = 10^{-12}$ V m^{-2} s^{-1} limited by trapping caused by $P3HT^+$:O_2^- complexes,[17] and holes, with a mobility of $\mu_p = 10^{-8}$ V m^{-2} s^{-1}.[18,19] We note that the same effect

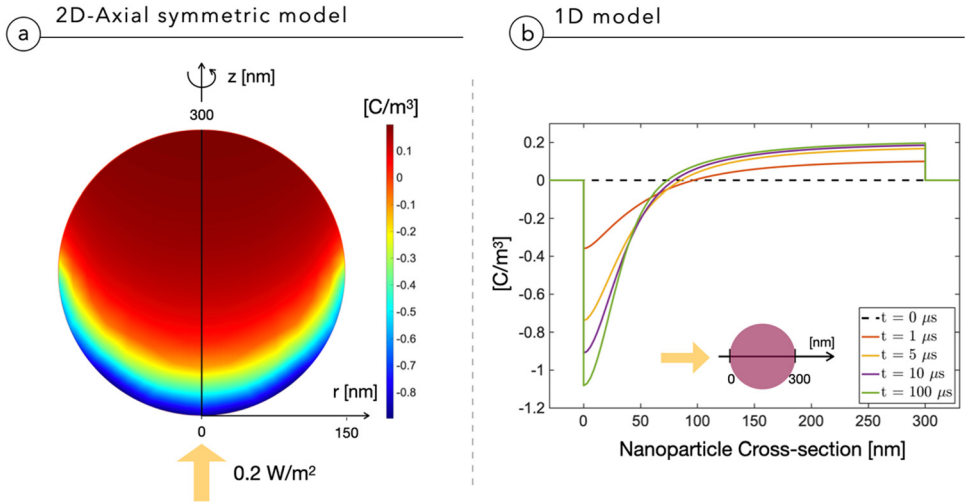

Fig. 2 Charge density distribution across the NP irradiated by a light intensity of 0.2 W m^{-2} impinging as depicted by the yellow arrow. (a) Results obtained using the 2DAS NP model. (b) Results obtained using the 1D-model as a function of time after the illumination.

well explains the electrochemical experiments on photovoltage in thin film electrodes.[4] The modeling reduction from a 2DAS to a 1D description returns coherent quantitative results: for the sake of simplicity and computational costs, when dealing with time-dependency and coupling with the biological system, we will preferentially use the 1D description.

The above-described NP polarization is not effective if the dielectric screening is at work. For this reason, the composition of the cleft region is crucial because it can enhance or completely hinder the screening effect. The first evidence for this phenomenon comes from a study of the normalized electric potential distribution around the NP in an empty medium with two distinct dielectric constants. 2DAS simulations of the steady state condition, reported in Fig. 3, show that a smaller dielectric constant of the surrounding medium corresponds to a larger region of the non-negligible electrical field, thus expanding the coupling range of the effect.

In other words, in the electrolytic aqueous environment, the polarized NP would be able to induce sizable polarization at the neuron membrane only if positioned at few Debye lengths from the interface. The estimated Debye length is $\lambda = \sqrt{\frac{\varepsilon_0 \varepsilon_r k_B T}{2q^2 I}} \simeq 9 \times 10^{-10}$ m, where ε_0 and ε_r are the absolute and relative dielectric constants of the aqueous medium, respectively, k_B is the Boltzmann constant, T is the temperature, q is the elementary charge and I is the ionic strength of the electrolyte. While the *in vivo* neuron/NP cleft is of several nm, it should be filled by proteins that decorate the NP (the so called "protein corona"[20,21]) and the neuronal membrane (adhesion proteins).[22] A protein aggregate has high resistivity[23] and would hamper ion penetration, contributing to create a "giga-seal" between the NP and the neuronal membrane that propagates electrostatic coupling.

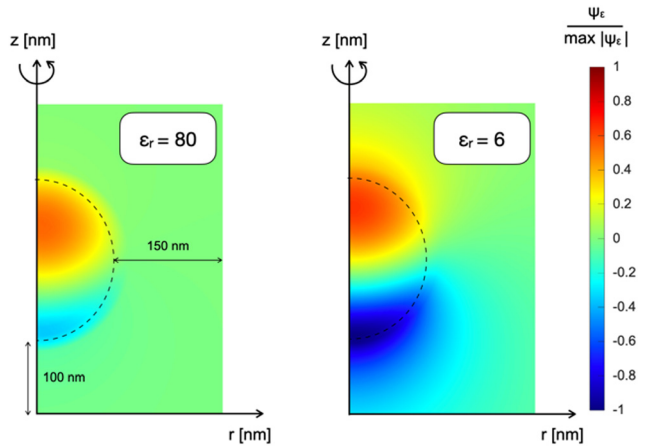

Fig. 3 Normalized electrostatic potential Ψ_ε distribution of a NP immersed in an empty medium characterized by different dielectric constants: on the left ε_r = 80; on the right ε_r = 6.

3.2. The electrostatic coupling mechanism

Once we consider that ionic screening would hamper electrostatic coupling, the next step is to include in the 1D model in the presence of protein islands that partially fill the cleft, creating "tunnels" of the same size of the cleft region, across which polarization may be transmitted.[22] To model this contribution also in the time domain, we applied the 1D time-dependent model (Section 2.1), which accounts for both the electronic transport across the NP and the ionic transport of bulk electrolytic ions in the aqueous regions.

While the bulk electrolyte properties are well described by the classic Poisson–Nernst–Planck model, the properties of the cleft were obtained with a modification of the classic drift diffusion transport. To describe the effect of the protein on ion migration, we introduced an additional term regulating the ion flux that depends on the protein space filling and push ions

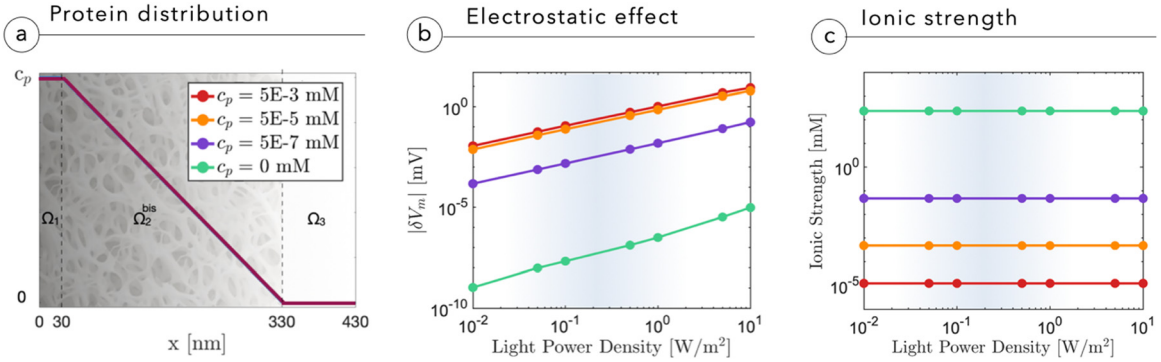

Fig. 4 (a) Cleft proteinic distribution across the electrolytic domain, where c_p may assume different values according to the simulated conditions. (b) and (c) Absolute value of membrane depolarization $|\delta V_m|$ (b) and ionic strength of the electrolyte (c) as a function of the light power density impinging onto the NP for various cleft proteinic concentrations.

towards empty space. This contribution does not depend on the charge sign of the ion, but it depends solely on the concentration gradient of the protein. The modified drift diffusion expression for the ion molar flux density J_α is:

$$J_\alpha = -\mu_\alpha \frac{z_\alpha}{|z_\alpha|} c_\alpha \left(\frac{\partial \psi}{\partial x} + \frac{1}{z_\alpha} \frac{V_{th}}{c_\alpha} \frac{\partial c_\alpha}{\partial x} + \frac{|z_\alpha|}{z_\alpha} \frac{V_{th}}{c_p} \frac{\partial c_p}{\partial x} \right) \quad (1)$$

where μ_α is the electric mobility of ion α, V_{th} is the thermal voltage, D_α is the ionic diffusivity, z_α is the ionic valence, c_α is the molar concentration of ion α, ψ is the electric potential and c_p is the protein concentration across the cleft. c_p has a given protein spatial distribution, reported in Fig. 4a. The detailed description and derivation are reported in the ESI,† eqn (S10).

The presence of a proteinic cleft, hampering the ionic screening, allows an efficient electrostatic coupling with the neuronal membrane, which is expressed and evaluated in terms of variations in membrane potential V_m. The membrane potential V_m is defined as the electric potential difference between the intracellular and extracellular compartments, that is, $V_m = \psi_N - \psi_{cleft}$, where ψ_N is the electric potential inside the neuron and ψ_{cleft} is the electric potential in the cleft adjacent to the membrane, *i.e.* $\psi(x = 0^+)$. In Fig. 4b, we report the absolute variation of the membrane potential $|\delta V_m| = |V_m^{off} - V_m^{on}|$ induced upon switching-on the light for 100 ms, as a function of light intensity and protein concentration in the cleft. Increasing the light intensity leads to an almost linear growth of $|\delta V_m|$. Electric field screening is quenched by the lack of mobile ions, until saturation sets in. The analysis shows that at $c_p \sim 10^{-5}$ mM, the magnitude of $|\delta V_m|$ becomes relevant at physiological light intensities, around 0.1–1 W m^{-2}. It is important to underline that the effect that we simulate is attributed to a single NP, whereas *in vivo* several tens of NPs constellate the neuron, thus providing multiple sources of depolarization around the membrane from the apical dendrite to the cell body. Also the effect of increasing size and micro-agglomeration, observed *via* high-resolution confocal microscopy in whole mount injected retinas,[2] may lead to an increase in the depolarization effect as shown in the study by Chiaravalli *et al.*[13] When light impinges on the neuron, the illuminated NP induces a negative potential in the cleft and reduces the membrane potential across the neuronal membrane, eliciting local depolarization. As light comes unidirectionally from the pupil, and the injected NPs remain concentrated in the outer retina without radially migrating to the inner layers,[1,2] electrical polarization will be the same for all NPs, which will negatively charge their side facing the membrane of bipolar and horizontal cells.

From Fig. 4b we also see that without a dielectric cleft, the electrostatic coupling with the neuron remains negligible even at the highest light intensities (green curve). Fig. 4c shows the expected reduction in ion concentration upon cleft filling by proteins.

3.3. The photo-chemical coupling mechanism

To identify potential alternative mechanisms, we also consider the chemical effect induced by the diffusion of O_2^- across the cleft and the subsequent chemical reactions of secondary species. Indeed, even in the secluded cleft space, chemical reactions could convert superoxide into hydrogen peroxide, a common reactive oxygen species (ROS), and in turn affect membrane components, including ion channels such as Transient receptor potential vanilloid 1 (TRPV1) channels.[24] Note that in our model, superoxide population is primarily a sort of "storage" of the charge. The negative oxygen ion is protected by a polaronic effect due to water molecule dressing that reduces back recombination. In the pseudo capacitive effect, superoxide molecules remain confined in the diffused interface and are doomed to recombine. Here we consider a different scenario in which the superoxide leaves the interface and diffuses in the cleft. If this happens, the conversion to ROS becomes a possible outcome of photostimulation.

Fig. 5a shows the O_2^- concentration, $c_{O_2^-}$, as a function of light intensity and protein concentration in the cleft. We find that different from the electrostatic coupling described above, the superoxide concentration is only slightly affected by cleft composition, whereas it is markedly dependent on the light intensity, as more electrons at the interface enhance the photocathodic production of O_2^-. At the physiological values of $\simeq$0.1–0.2 W m^{-2} light intensity and a time duration of 100 ms, the $c_{O_2^-}$ concentration increases by just few fractions

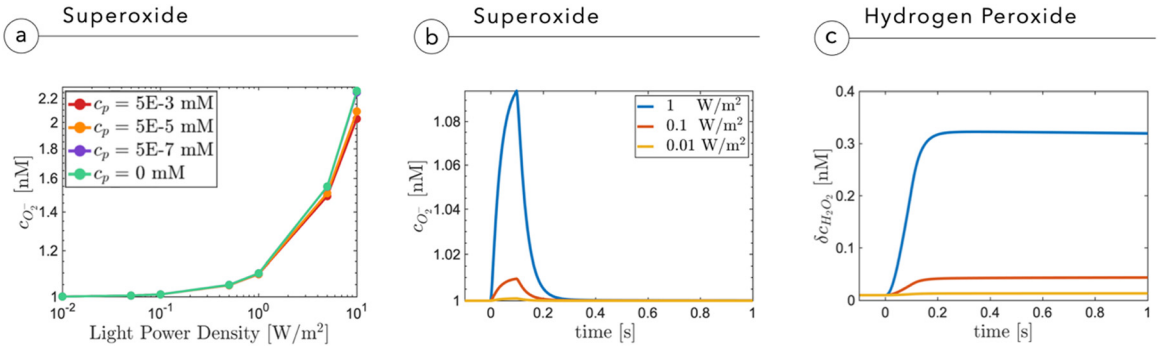

Fig. 5 (a) Superoxide concentration as a function of the proteinic concentration and the light intensity impinging onto the NP. (b) Profile of superoxide $c_{O_2^-}(0^+, t)$ as a function of time at different light intensities. (c) Variation of hydrogen peroxide concentration $\delta c_{H_2O_2}$ secondary to the production of superoxide.

of nM. The model also accounts for the ability of O_2^- to turn into hydrogen peroxide, whose concentration change secondary to a light pulse is reported in Fig. 5c. The concentration of hydrogen peroxide in the extracellular environment that can lead to oxidative eustress, (*i.e.*, a mild oxidative condition that is not harmful to cells), is estimated to be about 100 nM. This value, however, can be reached only at high light intensities, over 10 W m^{-2}.[24] We also look at the possible accumulation of hydrogen peroxide as a function of time, plugging in a reasonable value for its lifetime in the kinetics, as described in the ESI.† The simulated effect of a prolonged stimulation at physiological light intensities supports the negligibility of the photo-chemical effect under these working conditions (see below Fig. 7). In conclusion, our simulations suggest that the use of P3HT-NPs *in vivo* hardly induces any oxidative eustress at physiological light intensities for the retina, because both superoxide and hydrogen peroxide do not reach significant concentrations in the cleft region (above 100 nM[24]). Moreover, the effects on RGC firing of NPs injected subretinally in blind retinal explants were not affected by the blockade of TRPV1 channels by ruthenium red (ref. 2). Furthermore, the calculations argue against the risk of phototoxicity because toxic ROS concentrations ($\simeq$1000 μM) would only be reached at light intensities well above the damage threshold of the retina.

3.4. Pulsed light stimuli

Fixation eye movements, including tremor and micro-saccades, counteract image fading and keep modulating the light intensity impinging on retinal photoreceptors, even when the observer stares steadily. This effectively provides a pulsed-like illumination of retinal photoreceptors or, alternatively, of the implanted NPs.[25–27] In humans, the characteristic modulation time is in the order of 250 ms, while eye movement can be significantly faster, in the order of 10 ms. It is thus relevant to explore with specific time-dependent simulations the role of light pulse duration. As done before, for the sake of completeness, we will consider the build-up of superoxide as a fundamental agent in electrostatic coupling and the build-up of ROS, as a possible chemical agent.

Fig. 6a reports the cleft potential variation following light stimuli of increasing duration: after few tens of milliseconds, at 0.2 W m^{-2}, the potential reaches a plateau value and quickly recovers the initial value after switching-off the light. A similar trend is also observed by the superoxide concentration which, secondary to a prolonged stimulus, reaches an equilibrium value expressing the balance between its production rate at the NP interface and its evolution towards hydrogen peroxide (Fig. 6b). The observed plateau could in principle suggest that under prolonged exposure, hydrogen peroxide could build up to reach harmful concentrations. Fig. 6c shows that even for an

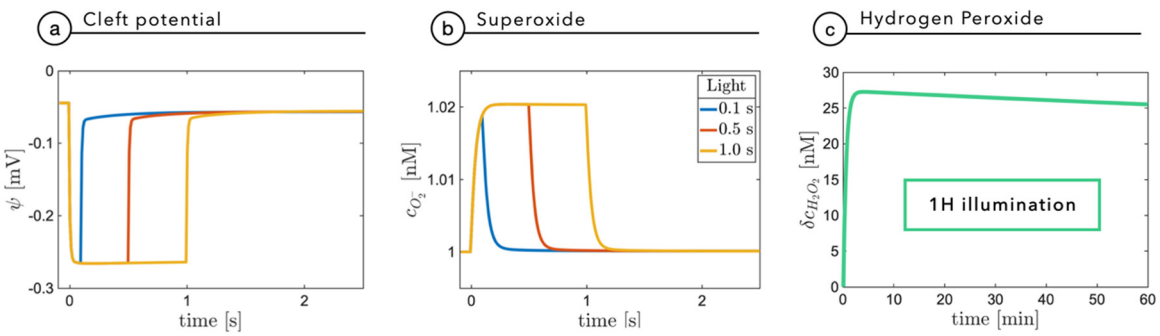

Fig. 6 Panels (a) and (b) show the simulation of the changes in the electric potential $\psi(0,t)$ and the superoxide concentration in response to light stimuli at a power density of 0.2 W m^{-2} for increasing durations from 100 ms to 1 s. Panel (c) illustrates the variation of the hydrogen peroxide concentration with respect to its equilibrium value after one hour of illumination.

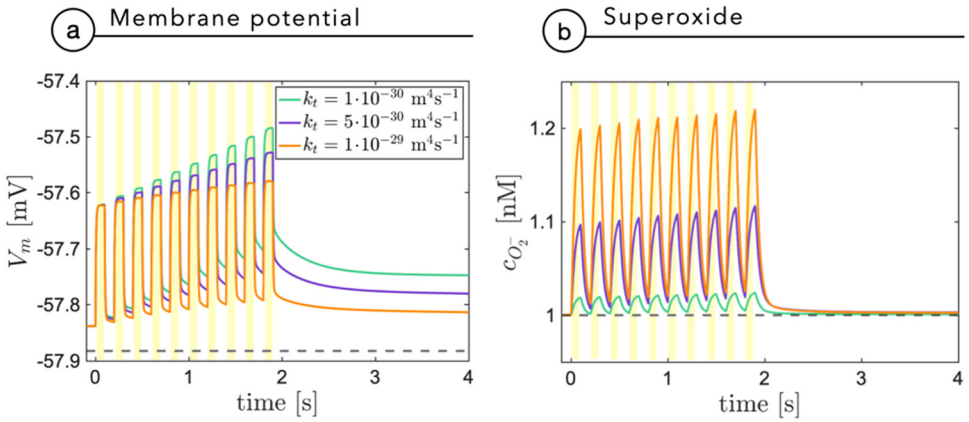

Fig. 7 The membrane potential (a) and the superoxide concentration (b) are shown as a function of time secondary to a train of light stimuli with an on/off duty cycle of 100 ms. The results are reported for three different values of the tunneling coefficient k_t, normally assumed equal to 10^{-30} m^4 s^{-1}, in agreement with the study by Rudolph *et al.*[28]

non-physiological, prolonged and continuous light stimulation, hydrogen peroxide concentration does not exceed 30 nM, remaining far below the threshold for extracellular perturbations (that is at least one order of magnitude higher).[24] These simulations again support the negligible and non-toxic role of the photo-cathodic behavior of P3HT-NPs within an oxygenated environment.

Fig. 7a shows the membrane potential as a function of time, during a train of light stimuli (100 ms each) with a 50% duty cycle with different values of the tunneling coefficient k_t, a parameter that rules the efficiency of the photo-cathodic production of superoxide that is employed in the description of the Marcus–Gerischer reaction at the P3HT/electrolyte interface. We find that k_t weakly affects the depolarization (Fig. 7a). The lower value, $k_t \approx 10^{-30}$ m^4 s^{-1} is in agreement with the data reported in the literature,[28] and it is associated with the lowest production of superoxide. We observe that sequential stimuli lead to the build-up of a small background signal, possibly caused by incomplete recombination. It is reasonable to think that the slow time-constant of plateau formation, combined with its small intensity, can be easily compensated by neuron transmembrane ionic exchanges. By increasing k_t, we see that the plateau is reduced. This can be ascribed to the reduced electrostatic effect localized in the NP and mainly caused by the pseudo-capacitive delocalization of the negative superoxide charge at the diffuse NP/cleft interface. The increased superoxide production is still below the concentration threshold for triggering physiological responses, as shown in Fig. 7b.

3.5. The role of the interface: experiment

A confirmation of our model comes from *ex vivo* experiments on blind retinal explants from RCS rats, a well-known rodent model of retinitis pigmentosa. P3HT-NPs were either injected in the subretinal space of acutely dissected naïve RCS retinas or injected *in vivo* in RCS rats to explant the retinas one month later, allowing the complete formation of the NP–bipolar cell interface. Although the light intensity required to stimulate an *ex vivo* response in dissected retinas is typically higher than that needed *in vivo*, a comparison of the two conditions at constant light intensity can provide an indication of the nature of the coupling phenomenon towards a full merging of the abiotic component with the biotic component. As reported in Fig. 8, the recordings of RGC firing on acutely injected explants displayed significantly smaller responses with respect to the retinas which experienced a prolonged (1 month) *in vivo* contact with the NPs before being explanted. In addition, the data spreading is much larger when testing post *in vivo* explants, towards high-rate numbers. This is true when looking at both the normalized firing rate (Fig. 8a and b) and the maximum firing rate (Fig. 8c). The difference in the response of chronically and acutely injected retinas can be ascribed to the distinct interface conditions that are established at NP/bipolar cell contacts: when the injection is performed *in vivo* one month before the explant, in addition to the formation of a protein corona on the surface of the NPs, the neuronal membrane response to the NP contact/docking can lead to the formation of a tight NP–cell interface that in turn enhances the resistive nature of the cleft. While the full *in vivo* biological response cannot be reproduced on explants studied *in vitro*, these results support the model described above and the proposed role of proteins in the cleft. Consequently, *in vivo* the transduction efficiency is enhanced by biological mechanisms that do not take place under *in vitro* or *ex vivo* experimental conditions.

4. Conclusions

Notwithstanding the remarkable success of the liquid retina prosthesis based on P3HT-NPs in rescuing vision in blind RP animal models, its working mechanism was incompletely understood.[1,2] By applying several mathematical models, we propose here a coherent picture of abiotic/biotic coupling, capturing the essential ingredients that describe the photostimulation mechanism responsible for the electrical activation of the inner retina by the injected NPs.

We explored both an electrostatic model and a photochemical model, finding that the two mechanisms reach the

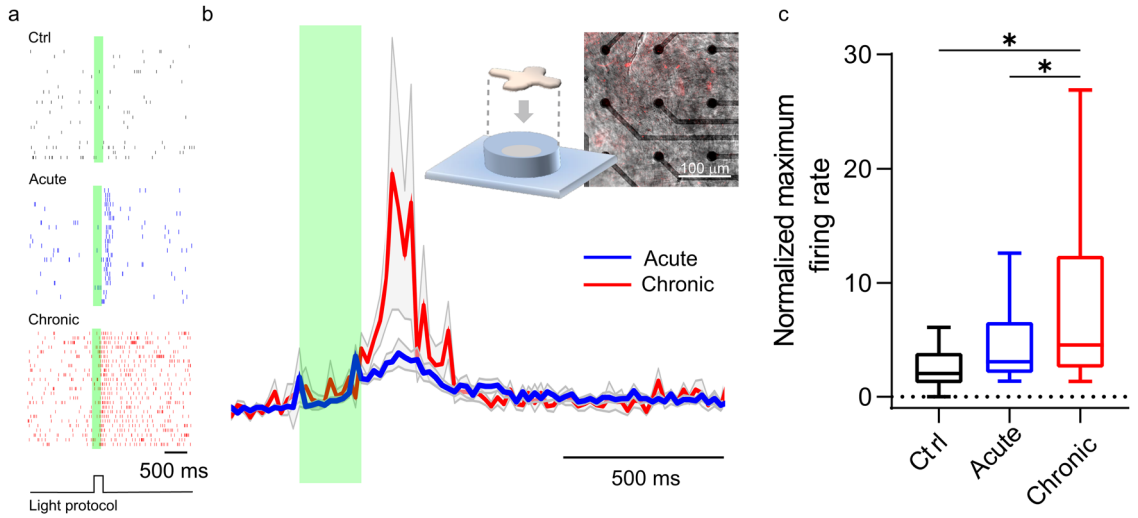

Fig. 8 (a) Representative raster plots in which vertical ticks represent the timestamps of action potentials recorded from retinal ganglion cells upon light stimulation in explants of untreated blind RCS retinas (Ctrl; top), in explanted RCS retinas acutely treated with P3HT-NPs (acute; middle) or in RCS retinas explanted from RCS rats that had been subretinally injected *in vivo* with P3HT-NPs treated *in vivo* 1 month before (chronic; bottom). The experimental protocol defines a pulsed light stimulation of 200 ms, indicated by the green transparent area, that is repeated 25 times (sweeps) at a frequency of 0.25 Hz. Each sweep corresponds to a row in the raster plot. (b) Time histogram (20 ms bin) of the normalized firing rate of acutely and chronically injected retinas when illuminated for 200 ms at a light power density of 20 mW mm^{-2} (λ = 530 nm). The inset shows a schematic representation of the experimental setup and the superimposition of the bright-field and fluorescence image of an explant on the MEA decorated by intrinsically fluorescent P3HT-NPs. (c) Quantification of the normalized maximum firing rate in untreated (Ctrl), acutely and chronically injected RCS retinal explants, showing an increased effect upon long-lasting contact of the particles with the retinal neurons *in vivo*. *$p < 0.05$, one-way ANOVA/Tukey's tests (n = 19, 105 and 38 neurons for Ctrl, acute and chronic, respectively, from at least 6 animals).

maximum efficiency under very different environmental conditions: (i) the photo-electrostatic effect is already relevant at physiological light intensities; (ii) the photo-chemical effect becomes relevant only at very high light intensities, far exceeding the physiological ones. This suggests that electrostatic coupling is the mechanism occurring during *in vivo* experiments and rules out possible phototoxic effects.

The pseudo-capacitive charging of the NP responsible for electrostatic coupling is appreciable only in the presence of a highly resistive cleft, where ionic screening is negligibly small (Debye length $\gg$ cleft thickness): if this condition is verified, even physiological light intensities (0.2 W m^{-2}) will be able to induce an appreciable depolarization of second-order retinal neurons. The high electric resistance of the medium filling the cleft is ascribed to its minimal thickness and to the presence of adhesion proteins of the neuronal membrane and corona proteins coating the NP. Therefore, the presence of the protein corona, in addition to neuronal adhesion proteins, is suggested by the model as a fundamental ingredient to ensure coupling among neurons and NPs at low light intensities. This introduces the concept of ''diffuse soft interface'', in contrast with the sharp boundary brought about by a metal electrode, validating the use of an organic semiconductor.

Experiments fully support this picture. Electron microscopy shows a cleft between a neuron membrane and a polymer nanoparticle that is less than 20 nm. Electrophysiology experiments show that the ''incubation'' time *in vivo* leads to sizable differences in the responses of blind retinas to light that can be reconciled by the *in vivo* formation of an efficient hybrid interface. These results also prove that *in vitro* experiments do not fully recapitulate the *in vivo* conditions, and that the prolonged contact between NPs and neurons, occurring *in vivo*, is necessary to build up a functional hybrid interface and fully elicit the physiological effects.

Author contributions

Chiaravalli performed the mathematical simulations and took lead in writing the manuscript. Sacco supervised the mathematical modeling contribution. Ravasenga and Jasnoor conducted *ex vivo* retina electrophysiology. Colombo performed data analysis, electron microscopy, supervision of the project and revision of the manuscript. Francia, Di Marco and Pertile performed surgery and *in vivo* nanoparticle microinjection. Lanzani and Benfenati conceived and supervised the project and revised the manuscript.

Conflicts of interest

There are no conflicts to declare.

Acknowledgements

The authors thank Drs M. M. La Vail (Beckman Vision Center, University of California San Francisco, CA) for kindly providing non-dystrophic RCS-rdy+ and dystrophic RCS rats; Angela Russo for her assistance in the subretinal microinjections;

M. Cilli and L. Emionite (IRCCS Ospedale Policlinico San Martino, Genova, Italy) for their assistance in surgical procedures. The research was supported by Fondazione Cariplo (project 2018-0505 to GL, FB and GP), H2020-MSCA-ITN 2019 ''Entrain Vision'' (project 861423 to FB and GL), EuroNanoMed3 (project Nanolight 2019-132 to FB), the Italian Ministry of University and Research (PRIN2020WMSNBL to FB and PRIN2020XBFEMS to GL), the Italian Ministry of Health (RF-2021-12374404 to FB, GP and GL) and IRCCS Ospedale Policlinico San Martino (Ricerca Corrente and 5 × 1000 grants to FB and EC).

References

1 S. Francia, D. Shmal, S. Di Marco, G. Chiaravalli, J. F. Maya-Vetencourt, G. Mantero, C. Michetti, S. Cupini, G. Manfredi, M. L. DiFrancesco, A. Rocchi, S. Perotto, M. Attanasio, R. Sacco, S. Bisti, M. Mete, G. Pertile, G. Lanzani, E. Colombo and F. Benfenati, *Nat. Commun.*, 2022, **13**, 3677.
2 J. F. Maya-Vetencourt, G. Manfredi, M. Mete, E. Colombo, M. Bramini, S. Di Marco, D. Shmal, G. Mantero, M. Dipalo, A. Rocchi, M. L. DiFrancesco, E. D. Papaleo, A. Russo, J. Barsotti, C. Eleftheriou, F. Di Maria, V. Cossu, F. Piazza, L. Emionite, F. Ticconi, C. Marini, G. Sambuceti, G. Pertile, G. Lanzani and F. Benfenati, *Nat. Nanotechnol.*, 2020, **15**, 698–708.
3 D. Mishra, S. Gade, K. Glover, R. Sheshala and T. R. R. Singh, *Curr. Eye Res.*, 2023, **48**, 208–218.
4 G. Chiaravalli, G. Manfredi, R. Sacco and G. Lanzani, *ACS Appl. Mater. Interfaces*, 2021, **13**, 36595–36604.
5 Y. He, R. Chen, W. Fa, B. Zhang and D. Wang, *J. Chem. Phys.*, 2019, **151**, 130902.
6 J. H. Byrne, *Postsynaptic Potentials and Synaptic Integration*, Elsevier, Amsterdam, 2014.
7 R. Shiells, *Photoreceptor-bipolar cell transmission*, Springer, Dordrecht, 1995.
8 G. Bondelli, S. Sardar, G. Chiaravalli, V. Vurro, G. M. Paternò, G. Lanzani and C. D'Andrea, *J. Phys. Chem. B*, 2021, **125**, 10748–10758.
9 J. F. Maya-Vetencourt, D. Ghezzi, M. R. Antognazza, E. Colombo, M. Mete, P. Feyen, A. Desii, A. Buschiazzo, M. Di Paolo, S. Di Marco, F. Ticconi, L. Emionite, D. Shmal, C. Marini, I. Donelli, G. Freddi, R. Maccarone, S. Bisti, G. Sambuceti, G. Pertile, G. Lanzani and F. Benfenati, *Nat. Mater.*, 2017, **16**, 681–689.
10 N. Martino, P. Feyen, M. Porro, C. Bossio, E. Zucchetti, D. Ghezzi, F. Benfenati, G. Lanzani and M. R. Antognazza, *Sci. Rep.*, 2015, **5**, 8911.
11 R. Sacco, F. Manganini and J. W. Jerome, *Mol. Based Math. Biol.*, 2015, **3**, 78.
12 D. L. Scharfetter and H. K. Gummel, *IEEE Trans. Electron Devices*, 1969, **16**, 64–77.
13 G. Chiaravalli, G. Lanzani and R. Sacco, *Photonics*, 2022, **9**, 710.
14 A. A. Moya, *Phys. Chem. Chem. Phys.*, 2015, **17**, 5207–5218.
15 M. A.-K. Urtenov, E. V. Kirillova, N. M. Seidova and V. V. Nikonenko, *J. Phys. Chem. B*, 2007, **111**, 14208–14222.
16 E. Arnault, C. Barrau, C. Nanteau, P. Gondouin, K. Bigot, F. Viénot, E. Gutman, V. Fontaine, T. Villette, D. Cohen-Tannoudji, J. A. Sahel and S. Picaud, *PLoS One*, 2013, **8**, e71398.
17 S. Bellani, D. Fazzi, P. Bruno, E. Giussani, E. V. Canesi, G. Lanzani and M. R. Antognazza, *J. Phys. Chem. C*, 2014, **118**, 6291–6299.
18 A. J. Mozer, N. S. Sariciftci, A. Pivrikas, R. Österbacka, G. Juška, L. Brassat and H. Bässler, *Phys. Rev. B*, 2005, **71**, 035214.
19 T. Agostinelli, M. Caironi, D. Natali, M. Sampietro, P. Biagioni, M. Finazzi and L. Duò, *J. Appl. Phys.*, 2007, **101**, 114504.
20 T. Kopac, *Int. J. Biol. Macromol.*, 2021, **169**, 290–301.
21 P. Breznica, R. Koliqi and A. Daka, *Med. Pharm. Rep.*, 2020, **93**, 342–350.
22 R. Changede and M. Sheetz, *BioEssays*, 2016, **39**, 1–12.
23 M. Natali, A. Campana, T. Posati, E. Benvenuti, F. Prescimone, D. O. Sanchez Ramirez, A. Varesano, C. Vineis, R. Zamboni, M. Muccini, A. Aluigi and S. Toffanin, *Biosens. Bioelectron.*, 2019, **141**, 111480.
24 H. Sies, *Redox Biol.*, 2017, **11**, 613–619.
25 R. G. Alexander, S. L. Macknik and S. Martinez-Conde, *Front. Neurol.*, 2018, **9**, 144.
26 F. F. Ghasia and A. G. Shaikh, *Exp. Brain Res.*, 2015, **233**, 1089.
27 R. Engbert and K. Mergenthaler, *PNAS*, 2006, **103**, 7192–7197.
28 M. Rudolph and E. L. Ratcliff, *Nat. Commun.*, 2017, **8**, 1048.

